

SIMULATED ENCOUNTERS OF PARKER SOLAR PROBE WITH A CORONAL-HOLE JET

MERRILL A ROBERTS,^{1,2} VADIM M URITSKY,^{1,2} C RICHARD DEVORE,² AND JUDITH T KARPEN²

¹*The Catholic University of America, 620 Michigan Ave. NE, Washington, DC, 20061*

²*Heliophysics Science Division, NASA Goddard Space Flight Center, Greenbelt, MD 20771, USA*

ABSTRACT

Solar coronal jets are small, transient features typically observed in coronal holes (CH). The upcoming Parker Solar Probe (PSP) mission provides the first opportunity to encounter CH jets *in situ* and clarify their internal structure and dynamics, necessitating a detailed grasp of a CH jet's defining characteristics. We present simulated PSP encounters with a CH jet, using projected PSP orbital parameters and a fully three-dimensional MHD model of a CH jet. We find that the three internal jet regions featuring different wave modes and levels of compressibility have distinct identifying signatures which could be detected by PSP. The leading wavefront of the jet and the plasma immediately behind it are characterized by a low density, trans-Alfvénic plasma flow, accompanied by the sudden onset of large-amplitude transverse velocity and magnetic field oscillations which are highly correlated in space and time. This region is shown to be purely Alfvénic, with the jet front itself showing characteristics of a fast switch-on type MHD shock. The lowest jet region appears as a compressible, non-Alfvénic region carrying most of the jet's mass. The region between the initial front and the dense region is mixed, sharing characteristics of the other two regions. We further examine a co-rotational encounter, holding the simulated spacecraft over the jet-producing region, to simulate PSP's co-rotational orbital phases, providing a comparison of all three jet regions.

Keywords: Sun: activity – Sun: corona – Sun:heliosphere – Sun: magnetic fields –
Sun:solar wind

1. INTRODUCTION

Solar coronal jets (Raouafi et al. 2016, and references therein) are small-scale, transient, highly collimated, impulsive flows of plasma that have been observed in all regions of the Sun. Due to the lower ambient emission from the cooler, low-density plasma prevalent in coronal holes, the Extreme Ultraviolet (EUV) and X-ray signatures of jets are more enhanced above background and therefore are more frequently observed in those regions. These coronal-hole (CH) jets typically exhibit structures with a wide base and a tall, spire or curtain of bright material (see Figure 1) in an ‘Eiffel tower’ or ‘ λ ’ geometry (see, e.g. Nisticò et al. 2009). Many CH jets have been observed by white light coronagraphs to propagate into the inner heliosphere (Wang et al. 1998; Wang & Sheeley 2002), and it has been suggested (Neugebauer 2012) that such CH jets may be the origin of microstreams detected *in situ* in the solar wind (Neugebauer et al. 1995). Observations have also detected in some CH jets distinctive fast-moving helical structures, which have been identified as radially outflowing nonlinear Alfvén waves (Cirtain et al. 2007). As nonlinear Alfvén waves have been detected in the interplanetary medium (Gosling et al. 2010; Marubashi et al. 2010), it is plausible that CH jets may be the source of some of these disturbances as well.

Due to the small scale and transient nature of CH jets, as well as the reliance on remote-sensing measurements, there remain many aspects of these coronal events that are not well understood. Among these are the jet’s interior structure and dynamics, and the extent to which the jet maintains its coherence as it propagate into the heliosphere.

In recent work, Karpen et al. (2017, hereafter K17) simulated a CH jet driven by magnetic reconnection following onset of a kink-like instability within the closed field of a minority polar-



Figure 1. SOHO/LASCO and SOHO/EIT images of a coronal jet that occurred on 2000 September 23 Wang & Sheeley (2002). Left panel: LASCO C2 difference image of the white-light jet. Right panel: EIT image of the EUV jet.

ity embedded in an otherwise uniform coronal hole. Their calculation included spherical geometry, solar gravity, and an isothermal wind, to examine the consequences for the propagation of the jet into the outer corona. The underlying kink-instability mechanism had been identified and studied extensively in a Cartesian, gravity-free environment by Pariat et al. (2009, 2010, 2015, 2016); see also Rachmeler et al. (2010).

Subsequently (Uritsky et al. 2017, hereafter U17), we investigated the internal structure and turbulent dynamics of the modeled jet, determining that there were three distinct regions within the propagating structure. (1) The immediate wake, behind the leading edge of the jet, is a region of incompressible flow moving at a speed comparable to the local Alfvén speed. (2) The dense jet, formed closer to the solar surface, is a region of compressible flow and overdense plasma moving at a much lower, but still supersonic, speed. (3) The remote wake is an intervening transition region where the other two regimes are mixed. This investigation showed that the model produces CH jets with complex internal dynamics and structure that are preserved as the jet propagates into the inner heliosphere. Thus, the results can be used to make

definitive predictions for extant and future observations of CH jets.

Parker Solar Probe (PSP, previously named Solar Probe Plus; Fox et al. 2016) is scheduled to launch in July 2018. PSP will obtain the first *in situ* measurements of the Sun closer than 0.3 AU, eventually approaching to less than $10R_{\odot}$ ($R_{\odot} = 7 \times 10^5$ km is the solar radius). The minimum periapsis of the spacecraft is currently planned at 5.9×10^6 km ($8.4R_{\odot}$), and its much-anticipated trip into the outer corona is expected to return a wealth of information. PSP is projected to reach its minimum perihelion in December 2024, when the Sun is predicted to be at solar maximum. Thus, the spacecraft is likely to encounter equatorial coronal holes and the ubiquitous CH jets that they contain. This raises the question: What observational signatures should be anticipated when PSP encounters a CH jet?

Our objective in this paper is to answer this question for the CH jet model simulated by K17 and analyzed by U17. We present the first virtual fly-throughs of PSP encountering a CH jet, using the PSP spacecraft trajectory in four dimensions (three spatial, one temporal) to develop predictions of the resulting signatures. We simulate PSP/jet encounters that probe each of the three regions described in U17, and determine the specific signatures expected for each type of encounter.

The paper is organized as follows. A brief description of the jet model is given in §2. We discuss the PSP mission in §3, and we describe the projected PSP orbital parameters and their interpolation into our model space in §4. The results of the three simulated fly-through trajectories are presented in §5. We summarize the implications of our findings and discuss future research in §6.

2. MODEL DESCRIPTION

The simulated coronal jet that we analyze in this study is a straightforward extension of

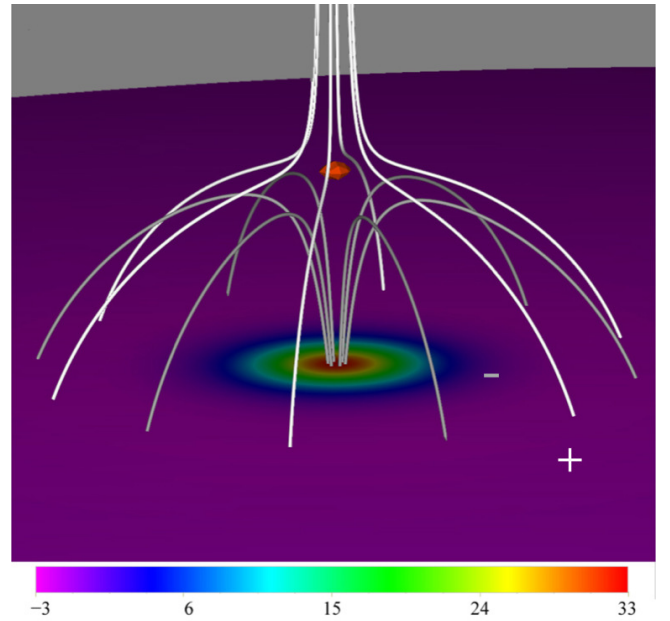


Figure 2. A view of the embedded minority polarity and the surrounding corona at $t = 0$. Color scale denotes the magnitude and sign of the radial magnetic field at the solar surface in Gauss. White and gray curves respectively show lines in open and closed flux systems, indicating the location of the separatrix surface, with the plus and minus symbols marking the opposing polarities. The region encompassing the magnetic null point of the system is shown as a closed red surface suspended between the two flux systems.

the simulation performed by K17 and analyzed further by U17. For convenience, we summarize the main features of the simulation below, but refer the reader to K17 for more details. Three simple changes were needed for this study. First, the original domain spanned the outer corona only to $9R_{\odot}$ and the jet propagated to only about $5R_{\odot}$; in order to develop predictions for PSP in the inner heliosphere, we extended the domain to $60R_{\odot}$ and allowed the jet to propagate out to about $35R_{\odot}$. Second, the original simulation allowed the adaptive grid to refine to a spacing as small as $5 \times 10^{-4}R_{\odot}$ at the solar surface and throughout the body of the jet, and the number of grid cells increased by more than a factor of 10 over the course of the simula-

tion. For the present study over the much more extended domain and a more extended duration of the event, we doubled the allowed minimum grid spacing to $1 \times 10^{-3} R_{\odot}$ in the volume beyond about $1.1 R_{\odot}$; the number of grid cells still increased by nearly a factor of 5. Third, in the original simulation, the magnetic field was energized by steady, slow footpoint motions at the solar surface following an initial ramp-up phase from rest. Such steady driving will produce a sequence of homologous jets as the magnetic energy builds slowly, is suddenly released following the kink-instability onset, and then begins to build up slowly again (Pariat et al. 2010). To avoid generating a train of recurrent jets in the simulation for this paper, we added a ramp-down phase of the surface flows back to rest when the critical energy for kink onset was approached the first time. This change made no discernible difference in magnetic energy released and kinetic energy generated by the jet during its impulsive phase.

The full simulation domain in spherical coordinates is $[1R_{\odot}, 60R_{\odot}] \times [-9^{\circ}, +9^{\circ}] \times [-9^{\circ}, +9^{\circ}]$ in radius r , latitude θ , and longitude ϕ . This is the same angular extent as K17, but with the outer radial boundary moved to $60R_{\odot}$, as mentioned. The grid is uniformly spaced in the angular directions θ and ϕ and linearly spaced in r (uniform in $\ln r$). The inner and outer radial boundaries of the domain are open, while the four side boundaries are closed.

The time-dependent, ideal, compressible, isothermal, magnetohydrodynamic (MHD) equations for mass, momentum, and magnetic field were solved using the Adaptively Refined Magnetohydrodynamics Solver (ARMS; DeVore & Antiochos 2008). The PARAMESH toolkit (MacNeice et al. 2000; Olson & MacNeice 2005) managed the parallel computations and the adaptive grid refinement process, which targeted regions of relatively strong electric current density for better resolution. The plasma was

assumed to be isothermal ($T_{\odot} = 1.0 \times 10^6 \text{K}$), eliminating the MHD energy equation and providing a straightforward, efficient way to produce a background supersonic solar wind (Parker 1958). The remaining model parameters, such as the temperature (T_{\odot}) and base mass density ($\rho_{\odot} = 2.0 \times 10^{-13} \text{kg m}^{-3}$), were chosen to reflect routinely observed environmental conditions for solar CH jets.

The magnetic configuration of the jet-driving region is shown in Figure 2. A radially oriented background field, uniform in the transverse dimensions, was assumed ($B_b = -2.5 \text{G}$ at $1R_{\odot}$). A radially oriented magnetic dipole of opposite polarity (maximum $B_d = +35 \text{G}$ at $1R_{\odot}$) was placed at a depth $R_{\odot}/70$ below the solar surface. These superposed fields form a dome-shaped separatrix surface with a null point at the top of the closed-flux region, as shown in the figure, and a circular polarity inversion line (PIL) at the solar surface within. A slow rotational motion about the center of the embedded bipole was imposed inside the PIL in order to twist and energize the magnetic field under the separatrix. Eventually, the accumulated twist exceeded the threshold for kink instability, causing the field beneath the dome to topple and reconnect rapidly through the null point above the dome, driving the resultant CH jet along adjacent magnetic field lines. As mentioned above, the motion was first ramped up from rest (duration: 1000 s), then held fixed at peak speed (duration: 1500 s), and finally ramped back down to rest (duration: 1000 s). Thereafter, the plasma and magnetic field lines were held fixed at the surface. Meanwhile, nonlinear Alfvén waves and plasma flows generated by the violent kink-driven reconnection comprised the jet, which propagated away into the outer corona and inner heliosphere.

3. PARKER SOLAR PROBE

PSP is scheduled to launch in July 2018 and become the first spacecraft to provide *in situ*

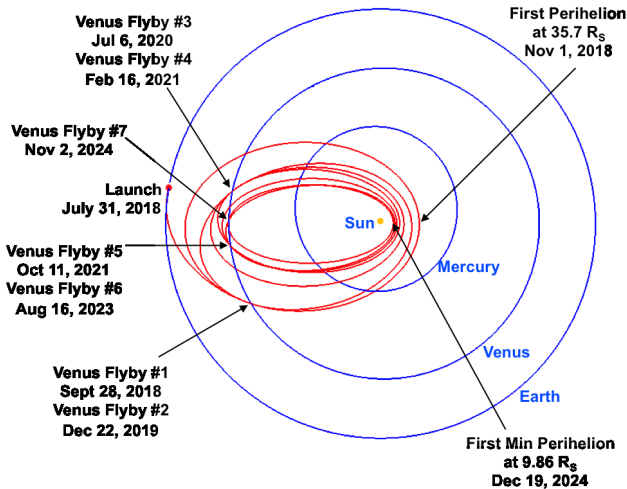


Figure 3. Illustration of PSP’s planned trajectory from Fox et al. (2016). The red line traces the orbital path, and the blue circles show the orbits of Mercury, Venus, and Earth. The elliptical PSP orbits become more eccentric and reach progressively lower perihelia due to seven planned Venus gravity assists over the course of the mission.

measurements of the inner heliosphere within $10R_{\odot}$. It will take up an orbit nearly in the ecliptic plane and, with the help of seven Venus gravity assists, will reduce its perihelion altitude from initially $35R_{\odot}$ to eventually $8.4R_{\odot}$ over the course of the seven-year nominal mission. PSP is expected to spend a total of 937 hours inside $20R_{\odot}$ and 14 hours inside $10R_{\odot}$. The close approach and extended duration below $20R_{\odot}$ will allow PSP to measure the coronal conditions that drive the nascent solar wind and detect eruptive transients such as CH jets. The mission will carry four instrument science investigations: the Electromagnetic Fields Investigation (FIELDS; Bale et al. 2016) to measure electromagnetic fields and plasma-density fluctuations; the Integrated Science Investigation of the Sun (ISIS; McComas et al. 2016) to observe accelerated particles at energies from tens of keV to 100 MeV; the Solar Wind Electrons Alphas and Protons Investigation (SWEAP; Kasper et al. 2016) to obtain particle counts for electrons, protons, and helium ions; and the Wide-field

Imager for Solar Probe Plus (WISPR; Vourlidas et al. 2016) white-light telescope to image the corona and inner heliosphere. Figure 3 shows the orbital paths throughout the mission. The effects of the gravity assists on the orbital period, aphelion, and perihelion are displayed in Figure 4. Our study focuses on detections of density, velocity, and magnetic field during the final three orbits (22-24) in the mission, all of which occur after the final gravity assist and attain perihelia inside $10R_{\odot}$. These orbits begin in late 2024 and provide the best chance for PSP to encounter equatorial coronal holes. The Sun then will be approaching solar maximum, when equatorial coronal holes and the CH jets they contain are observed most frequently.

4. FLYING THROUGH THE MODEL

4.1. Grid Regularization

The adaptive grid utilized by ARMS is essential to resolve adequately important jet features in the model, but it presents formidable challenges during the analysis of those features. For this investigation, we determined that a regular grid was necessary in order to establish consistent spacecraft coordinates and properly analyze the physical properties of the simulated CH jet. The method had to regularize the grid while maintaining the accuracy of the irregularly gridded data. For its simplicity and strong weighting of nearest-neighbor points in determining the new grid values, we chose linear interpolation based on a Delaunay (1934) triangulation of the irregular points. This was implemented in the Interactive Data Language (IDL) using the *Triangulate* and *Trigridd* functions, as follows.

After selecting a given two dimensional slice of the model space at constant radius r , the irregularly gridded θ and ϕ coordinates were read into IDL. From this set of co-planar points, the *Triangulate* procedure constructs the Delaunay triangles using the ‘divide and conquer’ method (Lee & Schachter 1980). The procedure gen-

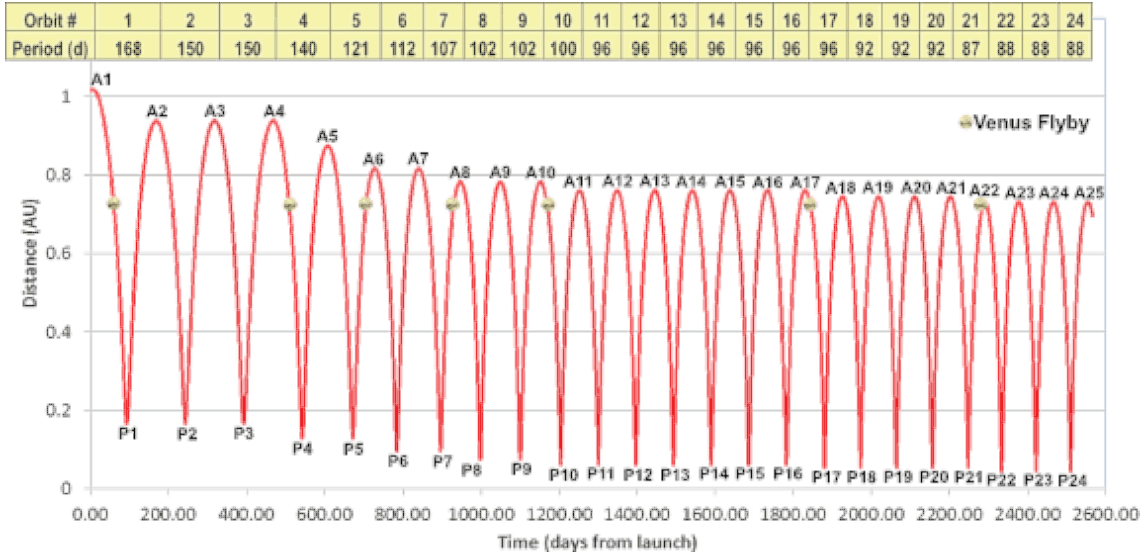


Figure 4. Distance vs. time for the PSP mission, from Fox et al. (2016). Each column gives an orbit number and period aligned with that orbit’s portion of the time/distance plot. A small image of Venus is placed at each point where PSP executes a gravity-assist maneuver. The aphelion and perihelion for each orbit are marked with ‘A’ and ‘P,’ respectively, and the orbit number.

erates a set of triangles from the given set of irregular points, such that a circle formed by connecting the vertices of any triangle does not contain any other point. This maximizes the minimum interior angle of the triangles and ensures that only nearby points are used to construct them. After they have been created, a spatially regular grid is overlaid on the triangles by the *Trigrad* function. The value at each point of this regular grid is given by a linear interpolation of the values of the vertices of the Delaunay triangle into which it falls. This ensures that the values used in the interpolation are those closest to the specified regular grid point, thereby minimizing the distortion of the original dataset. The complete procedure was performed at regularly spaced values of r and t ($\Delta r = 0.05R_{\odot}$ and $\Delta t = 25$ s) to build a uniformly gridded, four-dimensional dataset spanning the range of values required for a given fly-through trajectory.

4.2. Interpolated Orbital Trajectory

The trajectories that we use are derived from preliminary projected orbital parameters devel-

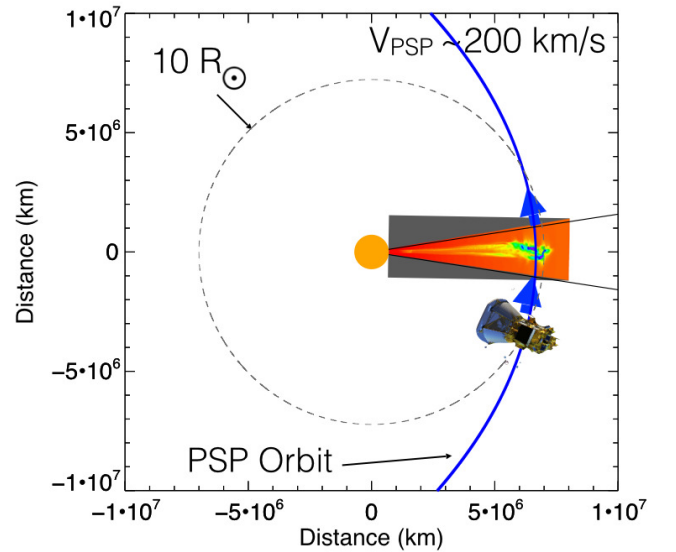


Figure 5. A section of the model space (red-orange wedge) superimposed over the fitted path of PSP during orbits 22-24 (blue ellipse). An image of PSP (not to scale) is shown moving in the direction of the arrows. An image of the Sun (to scale) and a grey dotted circle at $10R_{\odot}$ are shown.

oped by the PSP mission team (A. Szabo, personal communication). The dataset gives the

position of PSP once per day throughout the mission in Heliocentric Mean Ecliptic J2000 coordinates. We converted to spherical coordinates and rotated the domain so that the PSP orbital plane coincides with the $\phi = 0^\circ$ plane in our model space. Because the final three orbits (orbits 22-24) are nearly identical and the data points are sparse, especially near perihelion where the spacecraft moves most rapidly, data points from all three orbits were used to find a best-fit elliptical path, shown in Figure 5. We then restricted the path to the 18° angular size of our model space and interpolated data points along the path near perihelion corresponding to a data measurement cadence of 1 s at a spacecraft speed of 190 km s^{-1} , to emulate the conditions expected for PSP. The result was an array of spacecraft locations in spherical coordinates at 1 s intervals along the fitted elliptical orbit.

In the less than 9° -wide segment of PSP’s projected orbital path crossing the jet, the radial position r satisfies $9.516R_\odot \leq r \leq 9.541R_\odot$. The most recent PSP publications now project a minimum perihelion at $9.86R_\odot$ (see Fox et al. 2016, and Figure 3). Given the persistent structure of our CH jet and the relatively small change in perihelion (about 3.5%), this modification does not significantly alter the simulation results presented below.

4.3. Fly-Through Calculations

To simulate likely PSP jet encounters, four trajectories were studied: one passing through each of the three separate jet regions identified by U17 (see §5 and Figure 6 below), and one co-rotational trajectory that sampled the entire length of the jet. The first three encounter scenarios all have PSP flying along the elliptical arc through the model space described above, differing only in its start time during the simulation to sample the various regions. The simulated spacecraft followed its orbital path across the jet in each case. For each four-dimensional

spacetime position, the fly-through routine returns the model results at the spacecraft. The algorithm reads the time stamp of the spacecraft and opens the closest available time step from the model output. The radial coordinate of PSP is then read, and the appropriate surface of constant r is retrieved from the regularly gridded output. Next, the θ and ϕ trajectory coordinates are used to determine which model pixel currently contains the spacecraft. Finally, the data values at that pixel location are returned. This process is applied repeatedly to generate a time history for each variable along the PSP trajectory. It should be noted that the orbital path has a temporal cadence of 1 s, while the model output has a 25 s temporal cadence. This can result in the virtual spacecraft sampling the same pixel multiple times, even though it is temporally progressing through the model. In order to minimize this effect in the model output a 15s wide boxcar average is used to smooth the plot lines.

5. RESULTS

The schematic Figure 6 is adapted from U17, with the simulated PSP spacecraft trajectories shown as three solid blue arrows and the dashed blue line. The arrow trajectories sample the jet’s Immediate Wake (top arrow, earliest time), Remote Wake (middle arrow, intermediate time), and Dense Jet (bottom arrow, latest time) regions separately. The line trajectory is for a Co-rotational fly-through, in which the spacecraft hovers over a fixed location on the Sun and the jet passes over PSP, so the jet is sampled from the leading edge progressively through the other three regions, top to bottom. These four cases are discussed in turn.

5.1. Case 1: Immediate Wake

In this simulated encounter, the spacecraft samples the region directly behind the nonlinear Alfvén wave fronts that lead the jet (top blue arrow, Fig. 6). This is U17’s Immedi-

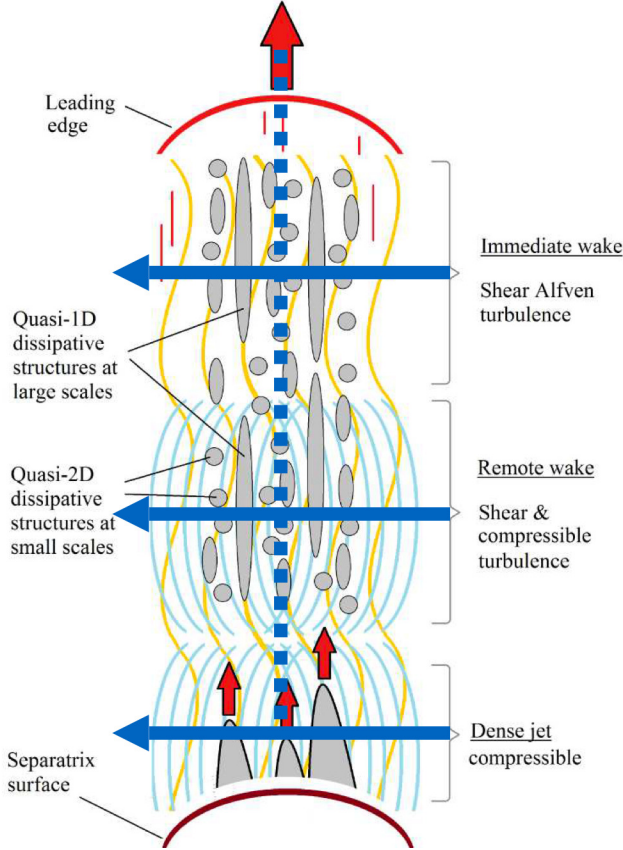


Figure 6. Schematic diagram showing the three regions of distinctive internal structure from the analysis of Uritsky et al. (2017). Red arrows mark the direction of plasma flow; blue arrows indicate schematically the three simulated PSP encounters through those regions. The dotted blue line illustrates the path of the corotational encounter and approximates the jet axis. Regions of Alfvénic and compressible wave activity are marked by yellow and light blue curves, respectively.

ate Wake. Figure 7 images the model space for $r \in [1R_{\odot}, 10R_{\odot}]$ and $\theta \in [-9^{\circ}, +9^{\circ}]$ at $\phi = 0$. Color shading renders the velocity magnitude, $|V|$. The simulated PSP spacecraft begins at coordinates $[9.54R_{\odot}, -4.5^{\circ}, 0^{\circ}]$ at time $t = 3900$ s, and follows the trajectory described above. The spacecraft first encounters the jet at time $t = 6137$ s, soon after Figure 7ii, and enters the region of highest flow speed at about 6300 s, shown in Figure 7iii. Subsequently, the spacecraft moves into a striated region of

lower speeds, in which local concentrations of enhanced velocity trail behind the leading front. PSP exits the jet at $t = 7681$ s, just after Figure 7viii. The spacecraft spends 1544 s inside the jet, which has a measured width $w \approx 293,000$ km $= 0.42R_{\odot}$.

The simulated PSP in situ measurements for this encounter are shown in Figure 8. At $t \approx 6100$ s, the spacecraft encounters the jet boundary, defined as where the radial velocity V_r is enhanced at least 20 km s^{-1} above the average steady background velocity of the radially flowing ambient solar wind. At the spacecraft altitude, the average background V_r is 192 km s^{-1} . As the spacecraft enters the jet, it passes into a region of enhanced V_r , rapidly increasing to more than an order of magnitude above the background solar wind radial velocity to a peak value of 2135 km s^{-1} . V_r seems to exceed the local Alfvén speed V_A (shown by the horizontal dashed red line in Figure 8a) inside the leading edge of the jet. However, when the speed is translated into the rest frame of the ambient solar wind, which is moving at a speed 192 km s^{-1} , the Alfvén Mach number $M_A = V_r/V_A \approx 0.97$. This indicates the presence of an Alfvénic shock front caused by the nonlinear, torsional Alfvén wave released at jet initiation, as seen also in the K17 jet, and moving at approximately the expected local Alfvén speed. In the region where V_r increases to the local Alfvén speed, the local magnetic field vector is strongly deflected from the radial direction by the non-linear wave (Fig.8f). As a result the radial magnetic field approaches zero in this region, as seen in Figure 8e, in contrast to the rest of the simulation space both inside and outside the jet, where the radial component dominates. The change in the radial magnetic field B_r (see Fig 8e) is seen here to have a very clear temporal correlation to the radial velocity. While V_A apparently remains constant throughout the traversed region when compared to the jet velocity, it does

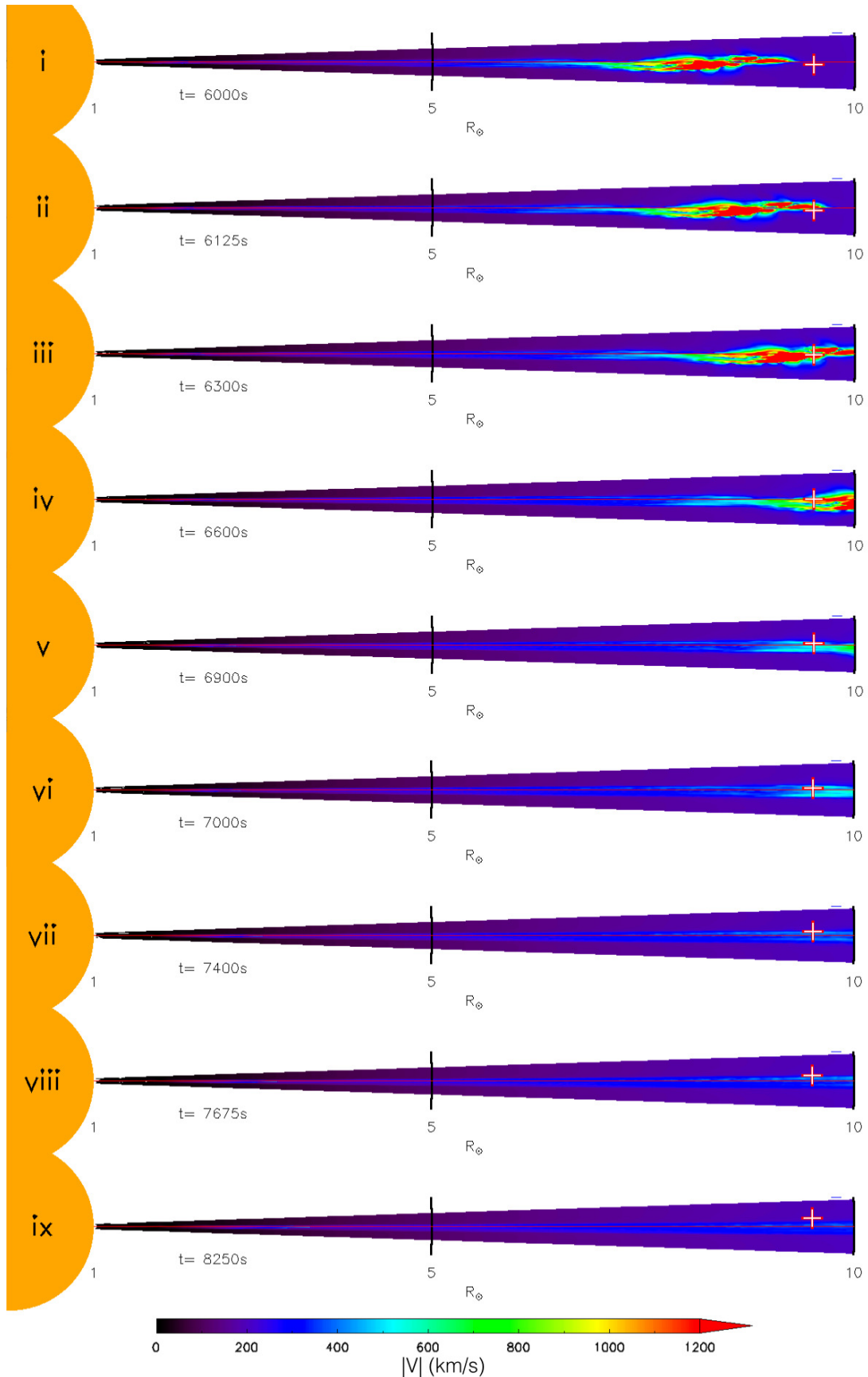


Figure 7. Case 1: Images of the simulated PSP encounter with a CH jet during the Immediate Wake fly-through. The red and white crosses mark the time-varying position of PSP. The images span $r \in [1R_{\odot}, 10R_{\odot}]$ and $\theta \in [-9^{\circ}, +9^{\circ}]$. Color shading denotes $|V|$. Each image (i,ii,iii, etc.) corresponds in time to the identically labelled grey vertical line drawn in Figure 8.

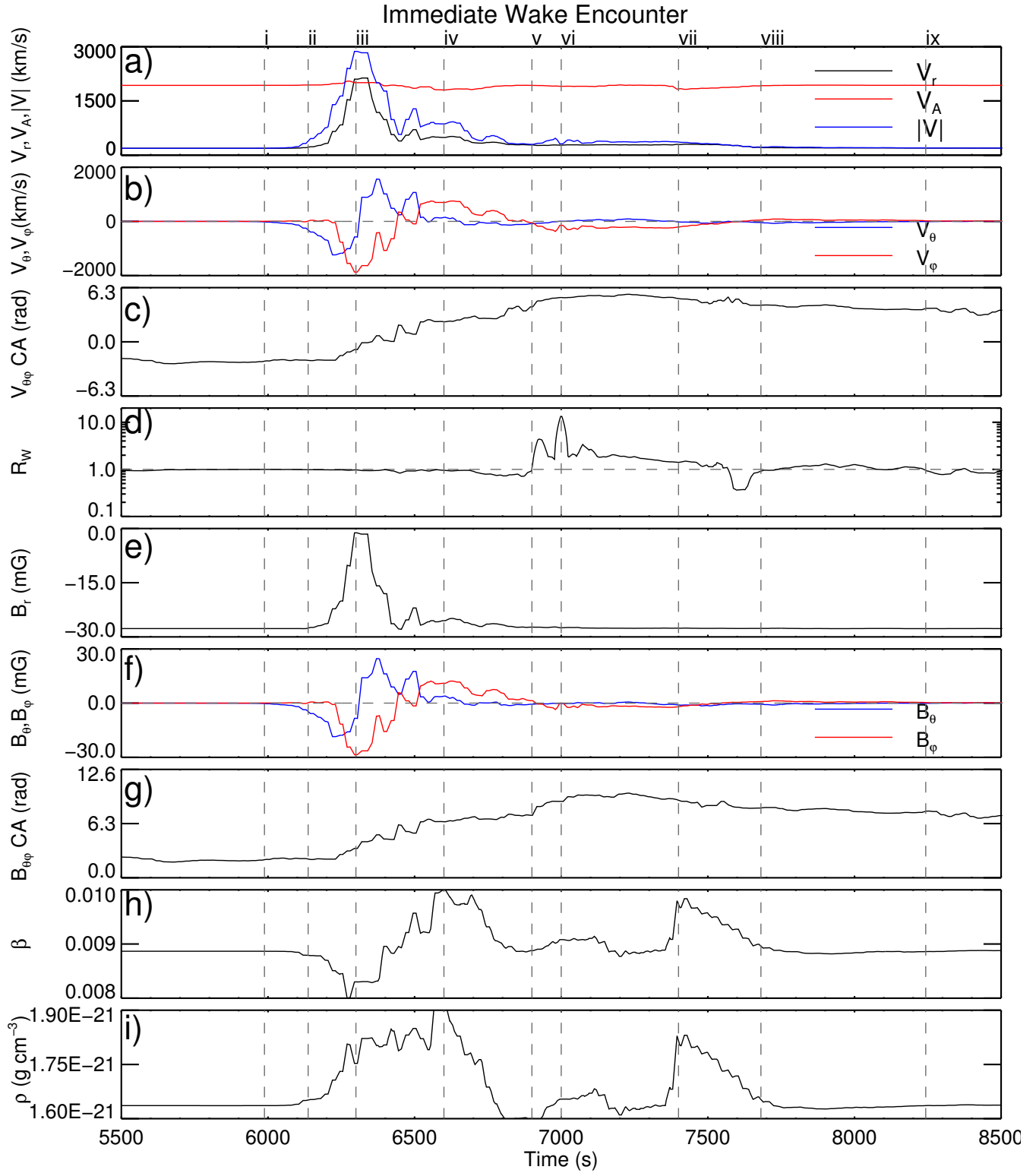


Figure 8. Time series of simulated PSP encounter with the CH jet leading wavefront and Immediate Wake. Each vertical gray line indicates a time at which an image is presented in Figure 7

in fact experience small variations due to the B-field fluctuations. These fluctuations are on a much smaller scale than that of the radial velocity, since the changes in B and $\rho^{1/2}$ are small and positively correlated, with the result that their ratio stays nearly the same.

This shock is also accompanied by the onset of velocity and magnetic field components transverse to the jet outflow (Fig. 8b),

$$V_{\theta\phi} \equiv (V_\theta^2 + V_\phi^2)^{1/2}, B_{\theta\phi} \equiv (B_\theta^2 + B_\phi^2)^{1/2}. \quad (1)$$

This onset of transverse components is also reflected in the clock angle (CA) of $V_{\theta\phi}$ and $B_{\theta\phi}$ vectors, as shown in Figure 8c. Here the clock angle remains steady until the encounter with the jet front, where it undergoes more than a full rotation from $t = 6200$ s to $t = 7200$ s. $V_{\theta\phi}$ and $B_{\theta\phi}$ are negligible upstream from the shock front, and suddenly take on large, non-zero values downstream from the shock. In addition, the magnetic pressure increases across the shock (and the correlated plasma β decreases), thus indicating a MHD fast-mode switch-on shock front (see, e.g. Kulsrud 2005), as deduced previously for the K17 jet (DeVore et al. 2016). These large values of $V_{\theta\phi}$ combine with the enhanced V_r to produce a maximum $|V|$ of 2872 km s^{-1} in the shock region.

The Walén (1944) number is the ratio of the transverse plasma flow speed to the Alfvén speed associated with the transverse magnetic field,

$$R_w \equiv (\mu_0 \rho)^{1/2} \Delta V_\perp / \Delta B_\perp. \quad (2)$$

For an ideal linear or nonlinear Alfvén wave in an isotropic plasma, $R_w = \pm 1$. As shown in Figure 8d, $R_w \approx 1$ throughout the encounter with the jet shock front and its immediate wake region. It deviates from this value beginning around $t = 6900$ s, when PSP emerges from the region of strongly enhanced $V_{\theta\phi}$ and $B_{\theta\phi}$. The average R_w in this region is $\langle R_w \rangle_{shock} = 0.955$, closely fulfilling the condition for a purely Alfvénic region in an isotropic plasma.

The spacecraft remains in a region of greatly increased V_r from $t \approx 6100 - 6900$ s. There are two successive enhancements in mass density and plasma β associated with strong excursions in R_w , one well above and one well below unity.

Thereafter, the virtual spacecraft remains in a region of slightly increased V_r until $t \approx 7700$ s, when the values of both the velocity and magnetic field return to levels comparable to those observed before the jet encounter. These results suggest an exterior sheath or envelope of mixed jet and ambient plasma, with small but finite transverse velocity and magnetic fields surrounding the jet. The virtual spacecraft spends about 900 s inside the strongly jetting plasma itself and 2200 s inside the surrounding jet envelope.

We note that all three components of the velocity are highly correlated with the corresponding components of the magnetic field (see Fig. 8a,b,e,f). This correlation also reinforces the conclusion that the immediate wake is a region of incompressible, purely Alfvénic flow. Density is enhanced by 18% over the background when the spacecraft passes into the jet region, accompanied by a dip in the plasma β (Figs. 8h,i), but this front does not carry the bulk of the jet's dense plasma with it. This ejected dense plasma is left behind by the Alfvénic wave front, as discussed below in 5.3.

To summarize, in the simulated encounter with the immediate wake, we found a sudden, simultaneous increase in all three velocity components as the spacecraft encountered the jetting region. There is no concurrent large increase in ρ , indicating that the wavefront is weakly compressible. A decrease in the radial component of the magnetic field (B_r) is observed simultaneous with and well correlated to the change in V_r . The onset of fluctuations in the transverse velocity ($V_{\theta\phi}$) and magnetic field components ($B_{\theta\phi}$) concurrent with the decrease in B_r and

a steady value of $|B|$ in this region is consistent with the angle of the magnetic field changing across this feature, suggesting that this wavefront is a weak switch-on type shock. Further, $V_{\theta\phi}$ and $B_{\theta\phi}$ show full rotations in their clock angle directions, revealing the helical interior structure of the jetting plasma. The Walén number (R_w) remaining at a value of +1 confirms that the plasma inside the immediate wake is Alfvénic and therefore incompressible.

5.2. Case 2: Remote Wake

The remote wake of the jet is a mixed region, as described in U17, which is less dynamic than the previous shock front and immediate wake. Figure 9 shows the spacecraft passing into and out of a jetting region which, while still distinguishable from the background solar wind flow, is significantly more homogeneous than the shock front and immediate wake that preceded it. The simulated PSP measurements are shown in Figure 10. The simulated PSP spacecraft begins at coordinates $[9.54R_\odot, -4.5^\circ, 0^\circ]$ at time $t = 7900$ s, and follows the calculated trajectory. PSP encounters the jet at $t = 8764$ s, and exits the jet at $t = 11822$ s, spending 3058 s inside the structure. This gives the jet a width of $\approx 581,020$ km $= 0.83R_\odot$. V_r increases from a background value of 194 km s^{-1} to a maximum of 320 km s^{-1} within the jet. The approximately 126 km s^{-1} enhancement in V_r (Fig. 10a) compared to the background is still measurable and significant, clearly indicating the boundaries of the jet.

In this case the fluctuations in $V_{\theta\phi}$ and $B_{\theta\phi}$ (Fig. 10b,f) are small and significantly less correlated than in the immediate wake region. There is a small-scale oscillation (with a period of about 330 s) which is well correlated at the beginning of the jet encounter, and becomes less so as the encounter progresses V_r in time. There is also a large-scale oscillation, most apparent in the B_ϕ component, which seems to indicate that B_ϕ varies spatially inside the jet, differing

in sign on either side of the jet’s approximate center. The clock angle for the transverse magnetic field (Fig. 10g) also shows a slow, large-scale rotation, while the $V_{\theta\phi}$ clock angle (Fig. 10c) shows more sporadic rotation. R_w in this region is initially close to 1, but deviates significantly from unity as the encounter with the jet continues (Fig. 10d), indicating that unlike the immediate wake, the remote wake is not a region of purely incompressible, Alfvénic flow. On the other hand, comparable to the immediate wake, the density ρ increases only 12% in this region, indicating that the plasma does not experience much compression here, either.

The correlation between the respective components of the velocity and magnetic field seen in the immediate wake is notably absent here, with the exception of the small-scale oscillations in the transverse components, whose periods appear to correlate quite well, especially in the early part of the encounter. These results support the conclusion of U17 that the remote wake is a mixed region which shares some characteristics of both the Alfvénic shock front and immediate wake ahead of it, and of the denser jet region that follows.

The predicted signatures of the remote wake encounter are more mixed overall. We still see a detectable increase in V_r , however here it is only ≈ 200 km s^{-1} above the background Parker wind, rather than the ≈ 2000 km s^{-1} seen in the leading edge and immediate wake. There is no significant change in B_r in this region and it is no longer strongly correlated to V_r , indicating that the plasma is now more compressional. Correlated large deviations in $V_{\theta\phi}$ and $B_{\theta\phi}$ are not present here, as mentioned earlier, however there is a small scale oscillation in the transverse components which is correlated strongly at the beginning of the encounter, though the correlation begins to fade near the end of the encounter. R_w varies during the encounter and is systematically below 1, indicating that this re-

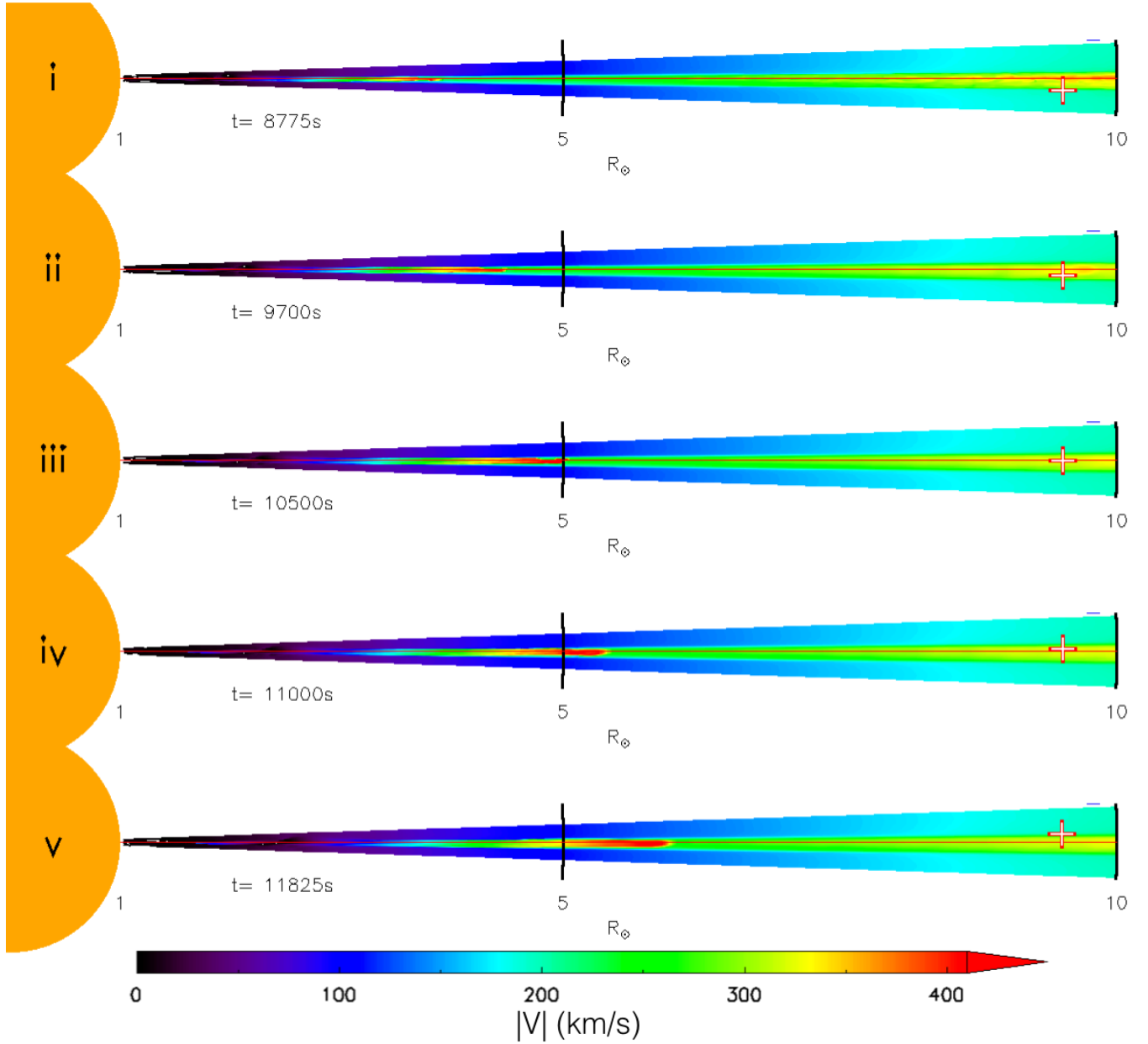


Figure 9. Case 2: Images of the simulated PSP encounter with a CH jet during the Remote Wake fly-through. The red and white crosses mark the time-varying position of PSP. The images span $r \in [1R_{\odot}, 10R_{\odot}]$ and $\theta \in [-9^{\circ}, +9^{\circ}]$. Color shading denotes $|V|$. Each image (i,ii,iii, etc.) corresponds in time to the identically labelled grey vertical line drawn in Figure 10.

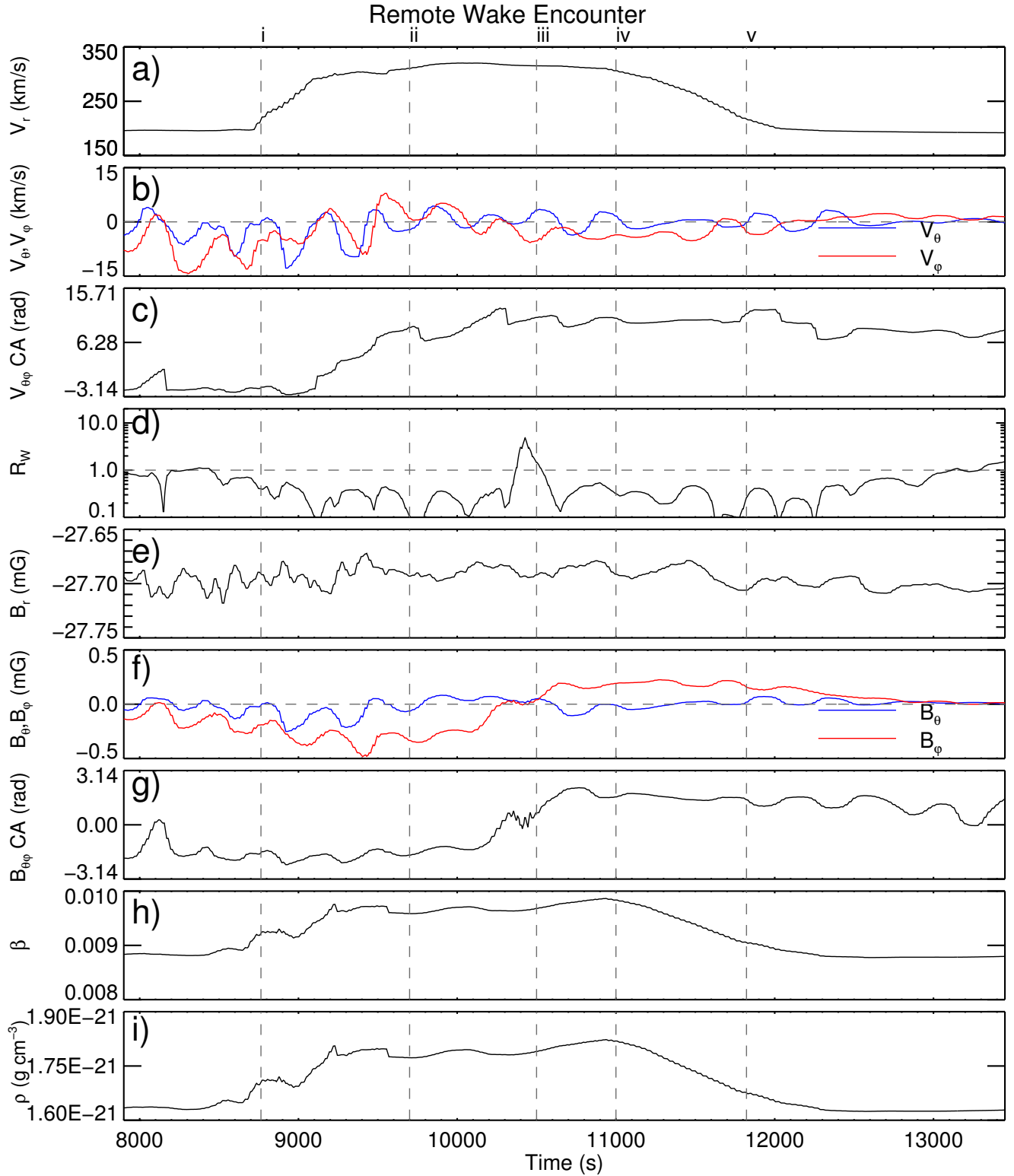


Figure 10. Time series of plasma variables for the Remote Wake fly-through. Each vertical gray line indicates a time at which an image is presented in Figure 9.

gion is no longer purely Alfvénic, and becomes even less so as later parts of the jet encounter the spacecraft. There is an increase in ρ concurrent with the enhanced V_r inside the jet, however this increase is small compared to the density of the upcoming dense jet region.

5.3. Case 3: Dense Jet

The dense jet region is the part of the jet structure typically observed by remote-sensing EUV and X-ray instruments. Figure 11 shows the spacecraft entering and then exiting the region of swift, dense jet plasma. As in the immediate wake, the plasma is faster at the leading edge of the dense region, but unlike the immediate wake, the dense jet region shows a more homogeneous velocity structure inside the jet, without any of the complex and spatially compact structure found in the shocked plasma of the immediate wake. The simulated PSP measurements are shown in Figure 12.

The simulated PSP spacecraft begins at coordinates $[9.54R_\odot, -4.5^\circ, 0^\circ]$ at time $t = 15400$ s, and follows the calculated trajectory. PSP enters the jet at $t = 16675$ s and exits the jet at $t = 20075$ s, spending 3400 s inside the jet. This gives the jet a width of $\approx 646,000$ km $= 0.92R_\odot$ at this point. In Figure 12a, V_r increases from a background value of 193 km s^{-1} to a maximum of 443 km s^{-1} within the jet. This 250 km s^{-1} enhancement in V_r is about twice that seen in the remote wake (although only 10% of the value of V_r in the immediate wake), and is correlated in time with the density enhancement (Fig. 12i), which is more than four times greater than the background solar wind density at this altitude. This is a much larger fraction than in the immediate or remote wake. Here $V_{\theta\phi}$ and $B_{\theta\phi}$ change very slightly, and appear to be completely uncorrelated to the radial magnetic and velocity fields (Fig. 12b,f). However the large scale oscillation in B_ϕ is still present, supporting the possibility discussed in §5.1 that B_ϕ varies persistently within the jet structure. The

clock angle of $B_{\theta\phi}$ (Fig. 12g) also supports this conclusion, as it completes a full rotation in the 5000 s plotted here. On the other hand, V_r and B_r (and therefore also β) correlate fairly well (see Fig. 8a,e,h), with the rise in B_r lagging the similar rise in V_r . The Walén ratio (R_w) is consistently less than one throughout the encounter by at least an order of magnitude. This, along with the large density increase, indicates that the spacecraft is in a more compressible plasma regime than in the other jet regions presented previously.

Hence the most striking signature of the dense jet is the fourfold increase in mass density clearly observed as the spacecraft enters the radially outflowing plasma, simultaneous with an enhancement in the radial velocity. As in the remote wake, the transverse components of both the velocity and magnetic field are small, and show no signs of cross-correlation.

5.4. Case 4: Co-rotational Encounter

This run examines a possible jet encounter during one of PSP’s co-rotational phases, where the spacecraft velocity is approximately equal to the rotational velocity of the solar surface, placing PSP temporarily in a heliostationary position. As noted in Fox et al. (2016), there will be two periods in each PSP orbit (one inbound and one outbound at $r \approx 35R_\odot$) where the spacecraft will be approximately co-rotational with the Sun. During these intervals PSP will perform fast radial scans, where the spacecraft will sample the solar wind over large radial distances while remaining over the same region of the solar surface. In order to model this configuration, we allowed our simulated spacecraft to ‘hover’ over the central region of the jet from $t = 3900$ s to $t = 21000$ s. This simulated co-rotational phase is both radially closer and of longer duration than the corresponding expected PSP co-rotational phase. However, this radial scan through all three major dynamic regions of the CH jet serves as a baseline for iden-

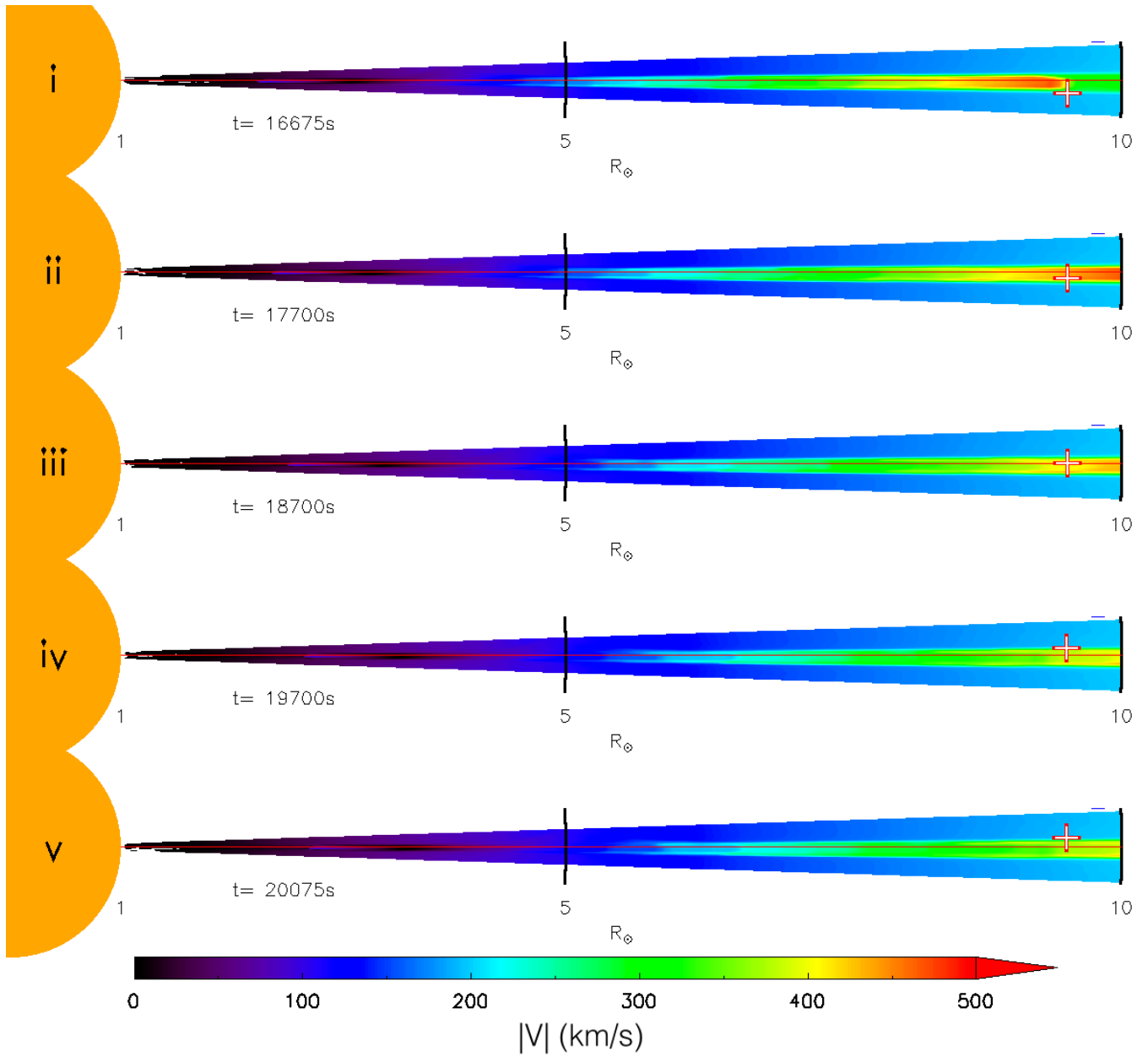


Figure 11. Case 3: Images of the simulated PSP encounter with a CH jet during the Dense Jet fly-through. The red and white crosses mark the time-varying position of PSP. The images span $r \in [1R_\odot, 10R_\odot]$ and $\theta \in [-9^\circ, +9^\circ]$. Color shading denotes $|V|$. Each image (i,ii,iii, etc.) corresponds in time to the identically labelled grey vertical line drawn in Figure 12.

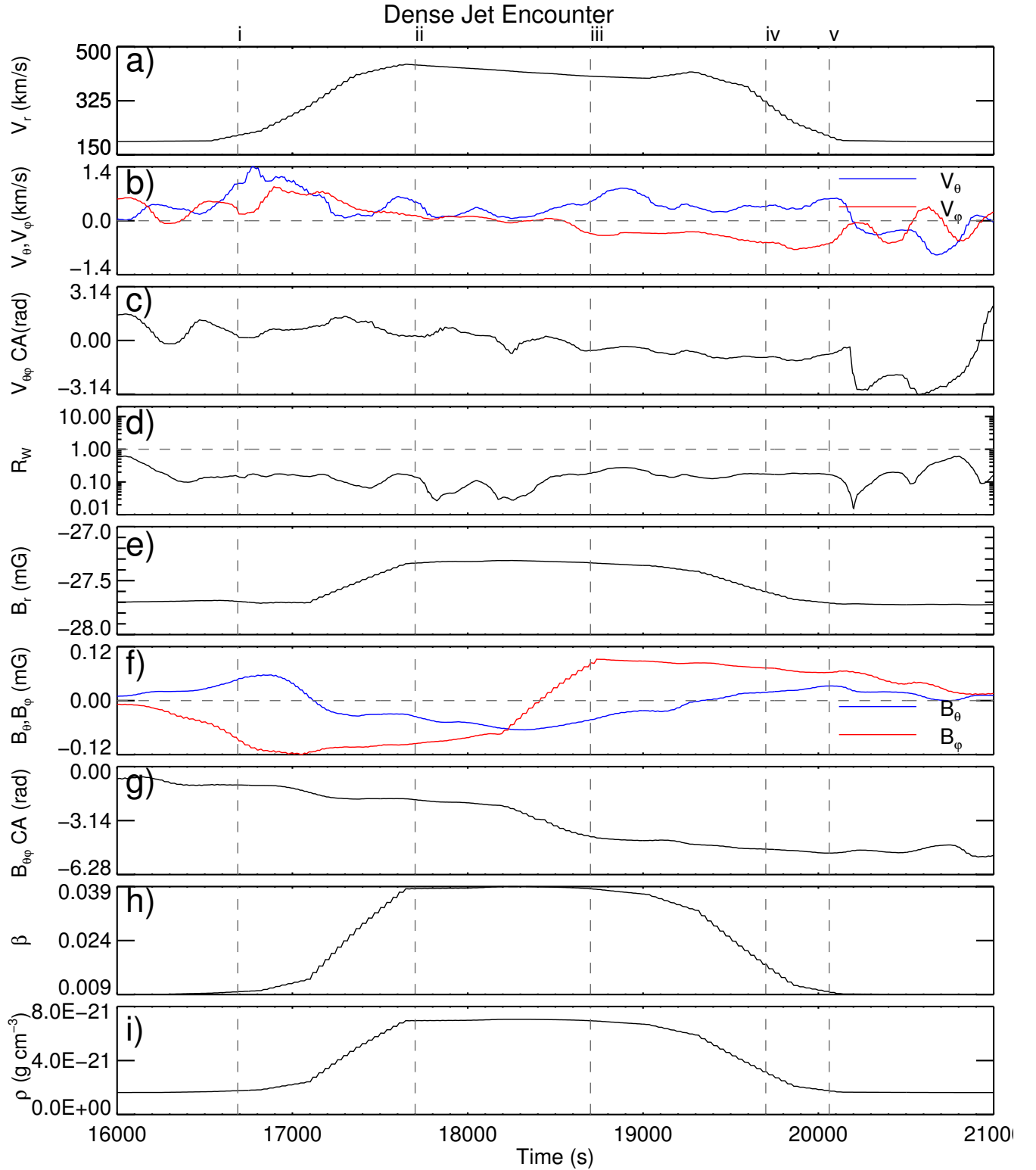


Figure 12. Time series of plasma variables for the Dense Jet fly-through. Each vertical gray line indicates a time at which an image is presented in Figure 11.

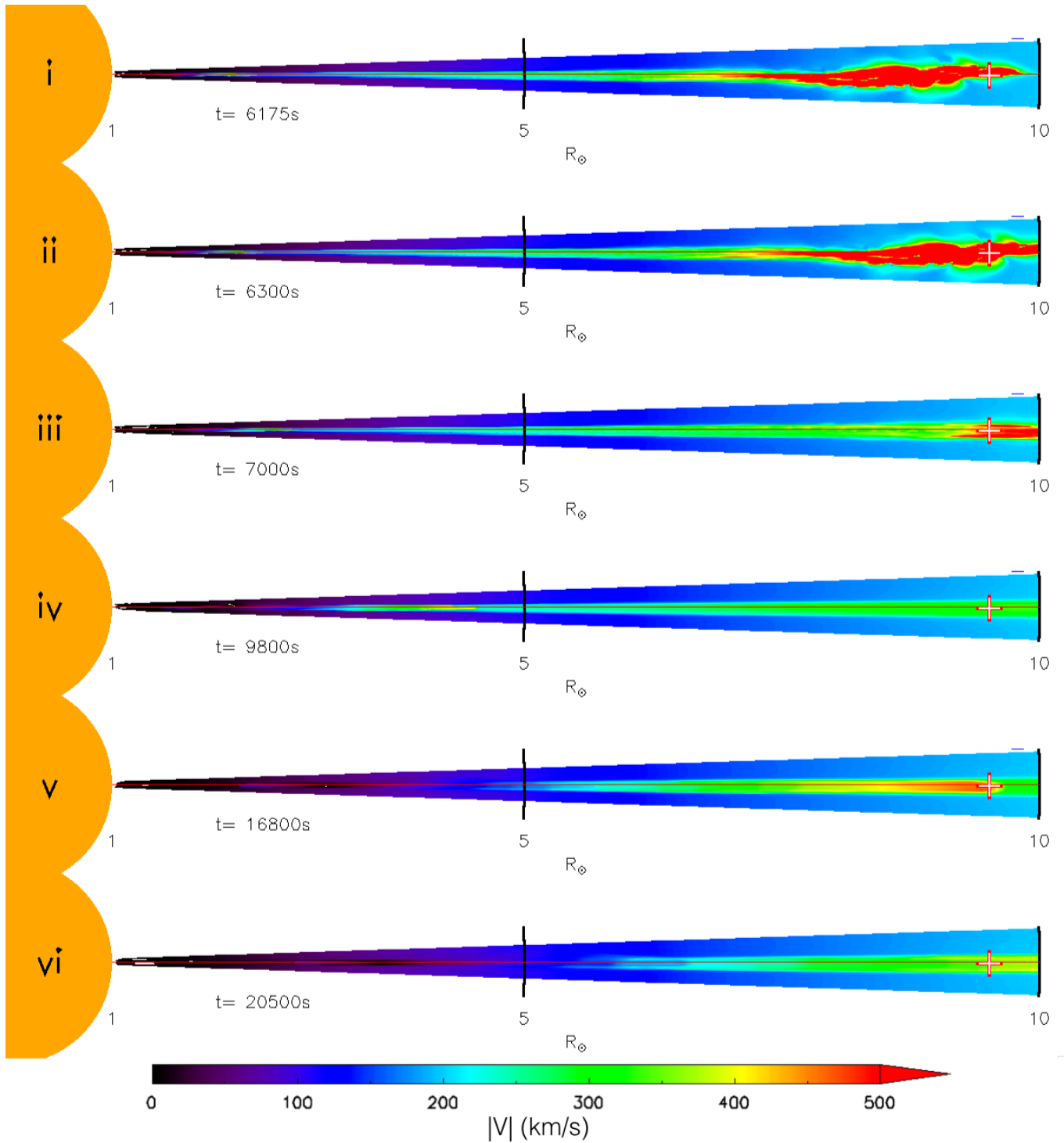


Figure 13. Case 4: Images of the simulated PSP encounter with a CH jet during the Co-rotational fly-through. The red and white crosses mark the time-varying position of PSP. The images span $r \in [1R_{\odot}, 10R_{\odot}]$ and $\theta \in [-9^{\circ}, +9^{\circ}]$. Color shading denotes $|V|$. Each image (i,ii,iii, etc.) corresponds in time to the identically labelled grey vertical line drawn in Figure 14.

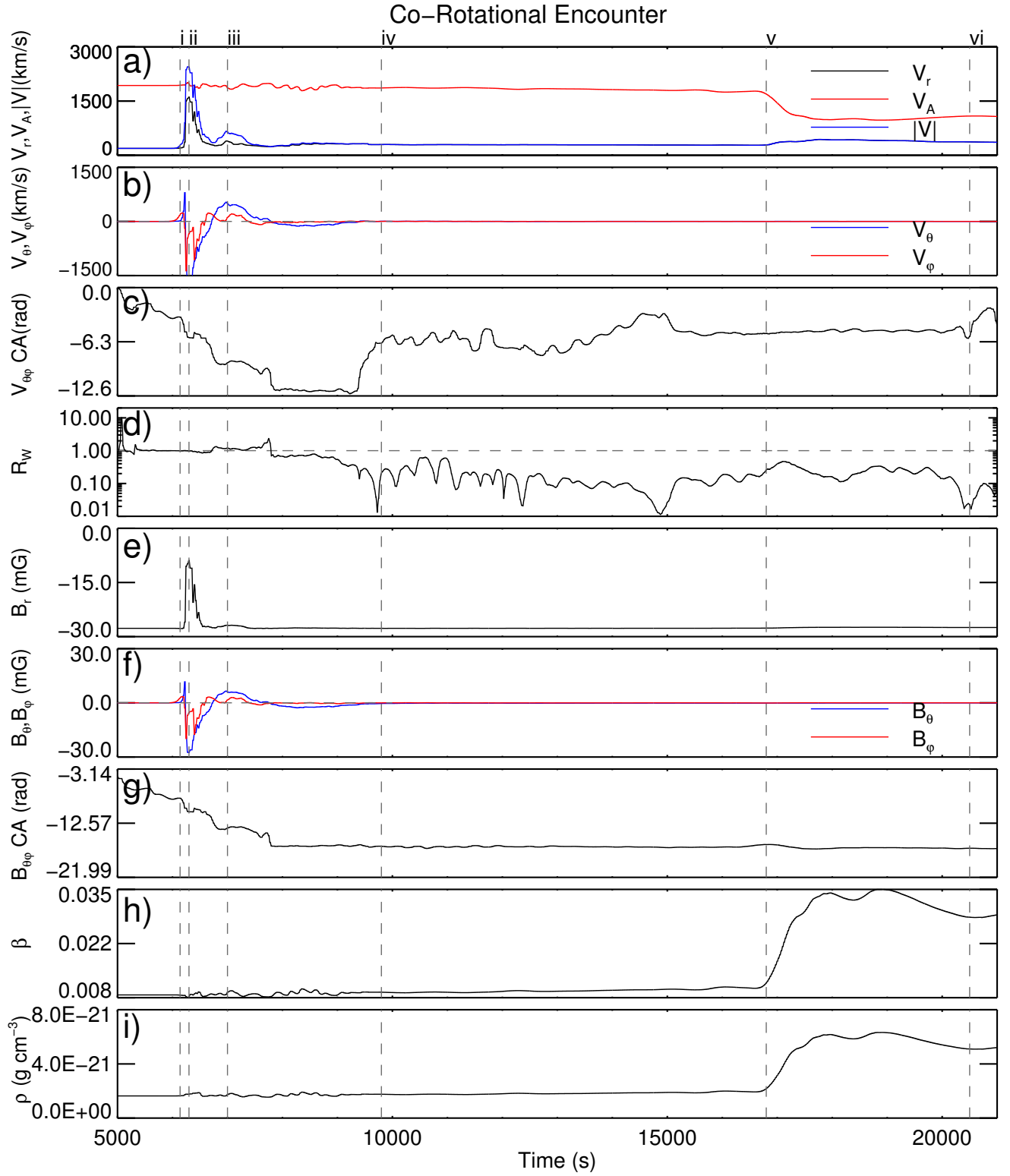


Figure 14. Time series of plasma variables for the Co-rotational fly-through. Each vertical gray line indicates a time at which an image is presented in Figure 13.

tifying features of jet crossings in PSP observations that may be of shorter temporal duration and/or higher altitude.

Figure 13 shows that all three of the previously studied regions pass over the spacecraft location: the immediate wake in 13a,b, the remote wake in 13c,d, and the dense region in 13e,f. Some features and trends interior to the extended jet are more apparent from this perspective than in the previous encounters. In Figure 14a the encounter with the high-velocity shock front at $t \approx 6100$ s is clear and correlates well with the immediate-wake encounter. An expected sudden drop in the Alfvén speed appears when the dense region is encountered, and this change correlates with the large increase in ρ found in Figure 13i. Figure 14 also confirms that while the mass density fluctuates modestly in the shocked plasma of the immediate wake, the bulk of the plasma is located in the lower, dense-jet region, which encounters the spacecraft at ≈ 16800 s. Figure 14b,f shows the sudden, correlated enhancement of $V_{\theta\phi}$ and $B_{\theta\phi}$ and the subsequent weakening of these components as the shock front moves farther away from the spacecraft. Figure 14d shows that R_w maintains a value of +1 during the entire encounter with the shock front and immediate-wake region, then deviates from this value throughout the rest of the jet. Thus, while the early part of the jet flow is incompressible and Alfvénic in nature, the subsequent regions are not. The clock angles of both $V_{\theta\phi}$ and $B_{\theta\phi}$ (Fig. 14c,g) show again that a full rotation of these vectors occurs in the immediate-wake region, and they progress toward a unidirectional configuration with only slight variations after exiting this region. It is interesting to note that this radial scan through the center of the jet reveals a ‘hollow’ jet structure, where ρ shows little enhancement, at least until an encounter with the lower altitude dense region. This renders two out of

our three jet regions difficult to detect remotely, reinforcing the need for *in situ* measurements.

As is seen most clearly in the co-rotational encounter, the internal plasma and field structures of the jet are generated at the reconnection site in the low corona, and then propagate outward after the jet launch. Although the leading front outpaces the dense plasma region, the jet maintains its coherent structure as it propagates radially outward. Our results suggest that an analysis of the jets encountered by PSP should reveal signatures persisting in the structure that illuminate the dynamics of the low-altitude regions that gave rise to the jet.

6. SUMMARY

In this paper we have shown results from a simulated PSP encounter with a fully 3D MHD model of a solar coronal hole jet. Our simulation begins with a closed bipolar region of magnetic field embedded in a unipolar region of otherwise open and radial magnetic field in a spherical, gravitationally stratified lower corona with a Parker solar wind profile. The simulation generates the free energy to produce a coronal-hole jet by slowly rotating this minority polarity region. The stressed flux eventually undergoes a kink-like instability in the magnetic field, and the subsequent reconnection drives a non-linear torsional Alfvén wave outward into the corona, followed by a slower moving spire of dense material.

Using the planned orbital parameters for the PSP mission, we constructed simulated spacecraft paths through the jet model region, and adjusted the start times so that the spacecraft would traverse each of the jet’s three regions. We also included a case where the spacecraft remains directly above the jetting region in order to simulate the co-rotational period that PSP is planned to experience on either side of perihelion. By modeling these encounters, we have shown that one dimensional fly-throughs like those PSP will perform can be used to gain

insight into the internal structure of CH jets, and we have shown that there are identifiable signatures of CH jets that can be detected *in situ* by PSP during its mission to explore the inner heliosphere.

Thus, our analysis suggests that the PSP mission will detect encounters with CH jets, with different signatures in differing jet regions. In the immediate wake of a coronal hole jet our analysis predicts a switch-on Alfvénic shock, as manifested by a sharp increase of the radial velocity approaching the local Alfvén speed, quick rotation of the magnetic field vector over an $\approx 2\pi$ angle, accompanied by a minor change in density, and with the Walén parameter remaining very close to the value of 1, signaling an incompressible plasma regime. When crossing the remote wake of the jet, an *in situ* probe would observe a less pronounced increase of the radial velocity, a more stable magnetic field vector, and a mixture of Alfvénic and compressional waves leading to a partial decoupling of velocity and magnetic field oscillations that grows with the distance from the Alfvénic jet front. The primary signature of the dense portion of the jet is a significant enhancement of plasma density and a dominance of compressional wave oscillations. All of these simulated fly-through signatures should be observable during the upcoming PSP mission.

In the future, it may be useful to refine both the interpolation of the spacecraft orbit and the

time cadence of the model output in order to investigate these features in more detail. On the other hand, the dynamics and structure of a CH jet, and especially of the Alfvénic shock front associated with it, should contain a multitude of kinetic-scale effects, such as temperature anisotropies, wave-particle interactions, plasma instabilities, and parallel electric fields, which can strongly influence jet evolution, and which are by definition not captured by MHD. Fortunately, PSP will be able to measure the physics at these kinetic scales, providing an unparalleled perspective into the true nature of these phenomena. We are excited about the possibilities the PSP mission presents, and look forward to the new scientific insights it will undoubtedly produce.

7. ACKNOWLEDGEMENTS

The authors thank Adam Szabo for providing the orbital coordinates used in this work. Also, MAR thanks S K Antiochos, S E Guidoni, P F Wyper, J T Dahlin, and M S Kirk for helpful conversations and feedback. MAR and VMU were supported by NASA grants NNG11PL10A 670.036 and 670.136 to CUA/IACS. CRD and JTK were supported by NASA LWS and H-SR grants to GSFC to investigate coronal jets and their heliospheric consequences. The numerical simulations were performed on Discover, the NASA Center for Climate Simulation computing system, under a NASA High-End Computing award to CRD.

REFERENCES

- Bale, S., Goetz, K., Harvey, P., et al. 2016, *SSRv*, 204, 49
- Cirtain, J. W., Golub, L., Lundquist, L., et al. 2007, *Sci*, 318, 1580
- Delaunay, B. 1934, *BAS*, 6, 793
- DeVore, C. R., & Antiochos, S. K. 2008, *ApJ*, 680, 740
- DeVore, C. R., Karpen, J. T., Antiochos, S. K., & Uritsky, V. M. 2016, in American Astronomical Society Solar Physics Division Meeting Abstracts #47, 03.09
- Fox, N. J., Velli, M. C., Bale, S. D., et al. 2016, *SSRv*, 20, 7
- Gosling, J. T., Teh, W.-L., & Eriksson, S. 2010, *ApJL*, 719, L36

- Karpen, J. T., DeVore, C. R., & Antiochos, S. K. 2017, *ApJ*, 834
- Kasper, J. C., Abiad, R., Austin, G., et al. 2016, *SSRv*, 204, 131
- Kulsrud, R. M. 2005, *Plasma Physics for Astrophysics* (Princeton: Princeton Univ. Press), 146
- Lee, D., & Schachter, B. 1980, *IJCIS*, 9, 219
- MacNeice, P., Olson, K. M., Mobarry, C., de Fainchtein, R., & Packer, C. 2000, *CoPhC*, 126, 330
- Marubashi, K., Cho, K.-S., & Park, Y.-D. 2010, in *Twelfth International Solar Wind Conference*, ed. M. Maksimovic, K. Issautier, N. Meyer-Vernet, M. Moncuquet, & F. Pantellini (New York: AIP), 240
- McComas, D., Alexander, N., Angold, N., et al. 2016, *SSRv*, 204, 187
- Neugebauer, M. 2012, *ApJ*, 750, 50
- Neugebauer, M., Goldstein, B. E., McComas, D. J., Suess, S. T., & Balogh, A. 1995, *JGRA*, 100, 23389
- Nisticò, G., Bothmer, V., Patsourakos, S., & Zimbardo, G. 2009, *SoPh*, 259, 87
- Olson, K. M., & MacNeice, P. 2005, in *Adaptive Mesh Refinement - Theory and Applications*, ed. T. Plewa, T. Linde, & V. G. Weirs (New York: Springer), 315
- Pariat, E., Antiochos, S. K., & DeVore, C. R. 2009, *ApJ*, 691, 61
- . 2010, *ApJ*, 714, 1762
- Pariat, E., Dalmasse, K., DeVore, C. R., Antiochos, S. K., & Karpen, J. T. 2015, *A&A*, 573, A130
- . 2016, *A&A*, 596, A35
- Parker, E. N. 1958, *ApJ*, 128, 664
- Rachmeler, L. A., Pariat, E., DeForest, C. E., Antiochos, S., & Török, T. 2010, *ApJ*, 715, 1556
- Raouafi, N.-E., Patsourakos, S., Pariat, E., et al. 2016, *SSRv*, 201, 1
- Uritsky, V. M., Roberts, M. A., DeVore, C. R., & Karpen, J. T. 2017, *ApJ*, 837, 123
- Vourlidas, A., Howard, R. A., Plunkett, S. P., et al. 2016, *SSRv*, 204, 83
- Walén, C. 1944, *ArA*, 30, 1
- Wang, Y.-M., & Sheeley, Jr., N. R. 2002, *ApJ*, 575, 542
- Wang, Y.-M., Sheeley, Jr., N. R., Socker, D. G., et al. 1998, *ApJ*, 508, 899